ACS APPLIED MATERIALS & INTERFACES

Research Article

www.acsami.org

High-Performance Lithium-Ion Cathode $LiMn_{0.7}Fe_{0.3}PO_4$/C and the Mechanism of Performance Enhancements through Fe Substitution

Bo Ding,[†,‡] Pengfei Xiao,[§] Ge Ji,[§] Yue Ma,[†,‡] Li Lu,*[,§] and Jim Yang Lee*[,†,‡]

[†]Center for Life Sciences (CeLS), NUS Graduate School for Integrative Sciences and Engineering (NGS), #05-01 28 Medical Drive, 117456 Singapore

[‡]Department of Chemical and Biomolecular Engineering, National University of Singapore, 10 Kent Ridge Crescent, 119260 Singapore

[§]Department of Mechanical Engineering, National University of Singapore, 9 Engineering Drive 1, 117576 Singapore

Supporting Information

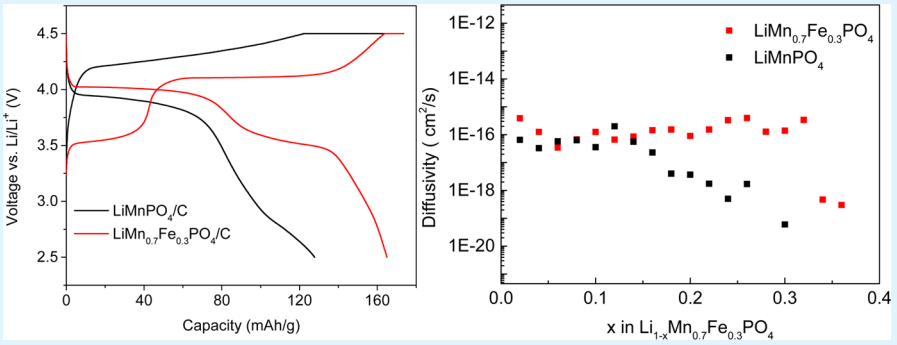

ABSTRACT: $LiMn_{1-x}Fe_xPO_4$/C (x = 0 and 0.3) with a uniform carbon coating and interspersed carbon particles was prepared by a high-energy ball-milling (HEBM)-assisted solid-state reaction. The as-synthesized $LiMn_{0.7}Fe_{0.3}PO_4$/C delivered an excellent rate performance as a $LiMnPO_4$ class of materials. Specifically, the specific discharge capacity was 164 mAh/g (96% of theoretical value) at the 0.05 C rate and 107 mAh/g at the 5 C rate (1 C = 170 mA/g). Electrochemical impedance spectroscopy (EIS) and galvanostatic intermittent titration technique (GITT) measurements indicated improvements in the transport of electrons and Li^+ as well as the emergence of a single-phase region in lithium extraction and insertion reactions.

KEYWORDS: *lithium-ion battery, cathode materials, solid-state reaction, mechanism, ion substitution*

INTRODUCTION

$LiMnPO_4$, like $LiFePO_4$, is a safe and environmentally benign cathode material that can be produced at a reasonable cost. The growing interest in $LiMnPO_4$ is primarily due to a theoretical energy density that is about 20% higher than $LiFePO_4$.[1−6] However, its sluggish transport of electrons and Li^+ transport is well-known, resulting in a rate performance far below the requirement for even small batteries. Similar to $LiFePO_4$, Li^+ diffuses in $LiMnPO_4$ mainly via the 1D channels parallel to the b axis.[7−9] During lithiation and delithiation, $LiMnPO_4$ undergoes phase transformation to $MnPO_4$. The large lattice mismatch between the $LiMnPO_4$ and $MnPO_4$ phases[10] presents a large energy barrier for Li^+ diffusion across the phase boundary.[11] Furthermore, strong localization of electrons and holes about the Mn centers[10,12,13] also renders polaron hopping between adjacent metal centers extremely difficult.

The performance of $LiMnPO_4$ should be improvable by collaborative bulk modifications and surface engineering. Toward this end, downsizing the primary nanocrystals on the nanoscale to reduce intraparticle-transport resistance and coating the nanocrystal surface with conductivity agent to reduce interparticle-transport resistance are the most common strategies.[14−17] Polyol synthesis,[14] solid-state synthesis in molten hydrocarbon,[16] and ball-milling-assisted solid-state reactions[17,18] have been used to prepare carbon-coated nanocrystalline particles. The increase in surface area with downsizing increases the amount of carbon greatly for a complete coverage of the nanocrystal surface. For example, Oh et al. reported as high as 30 wt % of highly conductive carbon was needed for optimal rate performance.[17] Such a large amount of carbon could, however, markedly reduce the energy density. Compared with size reduction and carbon coating, ion doping is an alternative to improve transport properties in the bulk without extreme size diminution.[19−21] Among the variety of elements that have been explored, iron-substituted $LiMn_{1-x}Fe_xPO_4$ solid solutions have thus far provided the best performance with the widest range of substitution (x from 0 to 1).[21−24]

Received: September 14, 2013
Accepted: November 5, 2013
Published: November 5, 2013

Ab initio calculations have shown that Fe substitution could increase the solubility limits of $LiMn_{1-x}Fe_xPO_4$ and $Mn_{1-x}Fe_xPO_4$ in each other to result in an expanded one-phase region and a contracted two-phase region.[25] Because lithiation/delithiation reactions in the one-phase region evade the sluggish kinetics of nucleation and growth of a new phase, an expanded one-phase region can improve the rates of delithiation/lithiation reactions. The size of the one-phase region depends on the Fe/(Fe + Mn) ratio, and calculations have shown that the range of solid solution is the widest with 15−30 mol % Fe substitution.[25] A composition of 30 mol % Fe substitution was chosen for this study. At this composition, the nanocrystal surface is populated with a large number of $Fe^{3+/2+}$ and $Mn^{3+/2+}$ redox centers that are more reactive than the $Mn^{3+/2+}$ redox centers in pristine $LiMnPO_4$. A faster exchange of Li^+ between the nanocrystal surface and the electrolyte may be expected. Furthermore, Fe doping also dilutes the Mn concentration. The resulting decrease in Jahn−Teller distortion caused by Mn^{3+} could also improve electron conduction in the bulk and consequently the rate performance in battery applications.

Despite the aforementioned advantages in theory, the experimental evidence for Fe substitution leading to actual performance enhancement is still rather limited.[14,19] In this study and using $LiMn_{0.7}Fe_{0.3}PO_4$ as an example, measurements by electrochemical impedance spectroscopy (EIS) and galvanostatic intermittent titration technique (GITT) confirmed the improvement in bulk transport properties after Fe substitution. Specifically, $LiMnPO_4$/C (the control) and $LiMn_{0.7}Fe_{0.3}PO_4$/C were synthesized by a scalable two-step solid-state reaction. The nanocrystals produced as such have a moderate crystallite size of about 50 nm, which ameliorated Li^+ diffusion in the solid state without the penalty of a large surface area (for carbon coverage). Carbon was introduced during the synthesis to integrate the nanocrystals electrically to reduce the external resistance to electron conduction.

EXPERIMENTAL SECTION

Materials Preparation. $LiCH_3COO{\cdot}2H_2O$, $FeC_2O_4{\cdot}2H_2O$, $Mn(CH_3COO)_2{\cdot}4H_2O$, and $NH_4H_2PO_4$ in amounts corresponding to the stoichiometry of $LiMn_{1-x}Fe_xPO_4$ (x = 0 and 0.3) and 10 wt % Super P carbon (Timcal) were mixed in acetone. This mixture was milled for 2 h in a stainless steel jar on a high-energy milling machine (SPEX 8000M), with a balls-to-material ratio of 10 to 1. The mixture after milling was dried at 80 °C for several hours to remove the acetone completely before the mixture was decomposed at 350 °C for 10 h in a flowing mixture of 5% H_2 in Ar. The decomposed mixture was ball-milled again for another hour in acetone with 10 wt % sucrose as a secondary carbon source. It was then subjected to a final heat treatment at 600 °C for 12 h to crystallize $LiMn_{1-x}Fe_xPO_4$ in flowing 5% H_2 in Ar.

Materials Characterization. The structural determination of $LiMn_{1-x}Fe_xPO_4$/C (x = 0, 0.3) was based on XRD using a Bruker D8 advance X-ray diffractometer and Cu Kα radiation (1.5405 Å). The morphology of $LiMn_{1-x}Fe_xPO_4$/C was examined by field-emission scanning electron microscopy (SEM) (on a JEOL JSM-6700F operating at 5 kV) and field-emission transmission electron microscopy (TEM) (on a JEOL 2100F operating at 200 kV). The carbon in the intermediate and final products was quantified by thermal gravimetric analysis in air from 20 to 800 °C using a Shimadzu DTG-60H.

Electrochemical Measurements. $LiMn_{1-x}Fe_xPO_4$/C (x = 0, 0.3), poly(vinyl difluoride) (PVDF) binder, and Super P carbon in a 80:10:10 weight ratio were mixed into a slurry in *N*-methyl-2-pyrrolidinone. The slurry was applied to an Al foil electrode and vacuum-dried at 120 °C overnight. The coated Al electrode along with a lithium foil counter and reference electrode with two sheets of Celgard 2400 separator between them were assembled in an argon-filled glovebox. The battery electrolyte was 1 M $LiPF_6$ in a mixture of ethylene carbonate (EC), diethyl carbonate (DEC), and dimethyl carbonate (DMC) (1:1:1 v/v/v) supplied by Hohsen Corp. Charge and discharge measurements were carried out on a Neware BTS-5V-MA battery tester. All cells were charged following a constant current constant voltage (CC−CV) protocol in the 2.5 to 4.5 V voltage range and discharged at different C rates (1 C = 170 mA/g). For the evaluation of rate capability, the test batteries were charged at 0.05 C to 4.5 V followed by potentiostatic charging at 4.5 V until the current decreased to 0.01 C. For the evaluation of cyclability, the test batteries were charged at 0.5 C to 4.5 V followed by potentiostatic charging at 4.5 V until the current decreased to 0.1 C. Cyclic voltammetry (CV) was performed in the 3.2 to 4.5 V voltage range at 0.05 mV/s on a μAutolab Potentiostat/Galvanostat. EIS was measured using a FRA type III attachment to the Autolab in the 100 kHz to 0.1 Hz frequency range and ±10 mV modulation. The Neware battery tester was also used for Galvanostatic intermittent titration technique (GITT) measurements, where charge and discharge was carried out at a low current density corresponding to the 1/20 C rate. For charging, the cell was charged for 24 min and then rested for at least 2 h until the voltage decay stabilized. A similar protocol was used for discharging.

RESULTS AND DISCUSSION

Figure 1 shows the XRD patterns of as-prepared $LiMn_{0.7}Fe_{0.3}PO_4$/C and $LiMnPO_4$/C. Both diffraction patterns

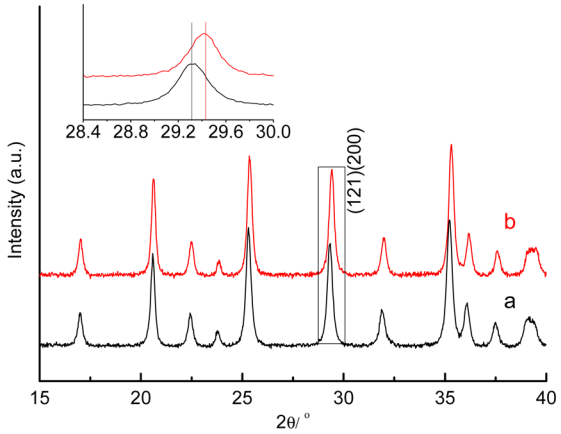

Figure 1. XRD patterns of (a) $LiMnPO_4$/C and (b) $LiMn_{0.7}Fe_{0.3}PO_4$/C; the inset shows the enlarged (121)(200) peak.

agree well with the orthorhombic *Pnma* space group. Because of the smaller ionic radius of Fe^{2+} (0.92 vs 0.97 nm for Mn^{2+}), the average M−O (M = Fe and Mn) bond length decreases after Fe substitution, shifting the diffraction angles to slightly higher angles (Figure 1, inset). The shorter average bond length decreased the ionicity of the Mn−O bonds in $LiMn_{0.7}Fe_{0.3}PO_4$ relative to the Mn−O bonds in $LiMnPO_4$, which could improve the electron polaron hopping between adjacent cationic centers. The broad diffraction peaks indicate that the crystallites in the as-synthesized materials were smaller than 100 nm according to the Scherrer equation. This appears to be a good size range in which the effect of Fe substitution can be detected and correlated with performance enhancements. Larger crystallites, with their increase in intraparticle-transport resistance, would be more likely to obscure the effect of Fe substitution.

The morphology of the as-prepared materials was characterized by SEM and TEM. The EM images in Figure 2 show

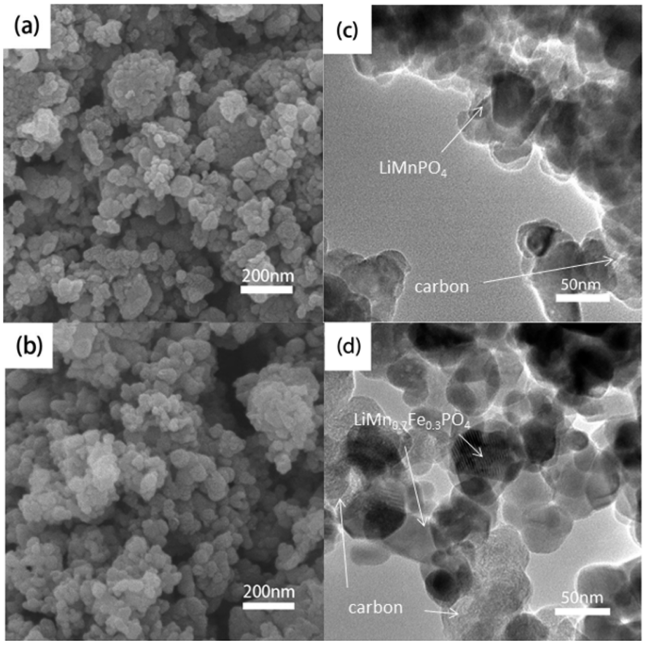

Figure 2. (a) SEM and (c) TEM images of $LiMnPO_4/C$; (b) SEM and (d) TEM images of $LiMn_{0.7}Fe_{0.3}PO_4/C$.

that the nanocrystallites of $LiMn_{0.7}Fe_{0.3}PO_4/C$ and $LiMnPO_4/C$ were about 50 nm in size. Some nanocrystals also agglomerated to form secondary structures. The nanocrystals were small enough to provide a sufficiently large surface area for Li^+ intercalation and carbon coating as well as short Li^+ diffusion and electron-hopping path lengths in the primary nanoparticles. The nanocrystals were interspersed with carbon particles, as shown in Figure 2c,d. The amount of carbon was determined to be 12 wt % for $LiMnPO_4/C$ and 12.2 wt % for $LiMn_{0.7}Fe_{0.3}PO_4/C$. The first ball milling in the synthesis dispersed the carbon particles as embedded current collectors. The second ball milling with sucrose followed by the decomposition of the latter increased the electrical integration between the embedded carbon particles and olivine phosphate nanocrystals. The embedded current collectors improved the efficiency of electron conduction between nanocrystals. At the same time, the pyrolysis of adsorbed sucrose formed a continuous carbon film on the nanocrystal surface, enabling electrons to be extracted from any part of the nanocrystal surface. The extracted electrons could then be shuttled through

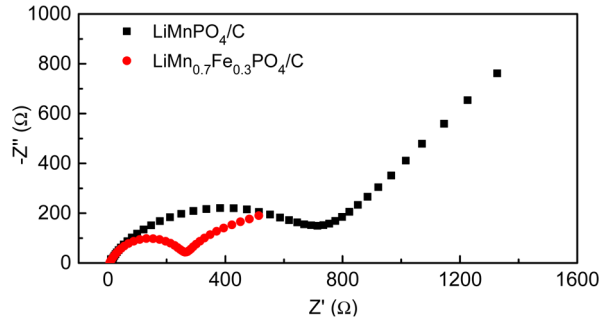

Figure 4. Nyquist plots of $LiMnPO_4/C$ and $LiMn_{0.7}Fe_{0.3}PO_4/C$ electrodes in test cells.

the dispersed carbon nanoparticles to the external current collector. The porosity between the nanocrystals and carbon nanoparticles enabled unhindered electrolyte percolation to wet the nanocrystal surface. Figure 3a shows the first cycle voltammograms of $LiMn_{0.7}Fe_{0.3}PO_4/C$ and $LiMnPO_4/C$. For $LiMn_{0.7}Fe_{0.3}PO_4/C$, there were two decoupled redox systems with oxidation peaks at 3.55 and 4.09 V, corresponding to the Fe^{3+}/Fe^{2+} and Mn^{3+}/Mn^{2+} redox couples, respectively. $LiMnPO_4/C$, however, displayed only one redox reaction with an oxidation peak at 4.13 V, corresponding to the Mn^{3+}/Mn^{2+} redox couple. The slight shifts in the Mn^{3+}/Mn^{2+} and Fe^{3+}/Fe^{2+} oxidation peaks in $LiMn_{0.7}Fe_{0.3}PO_4$ relative to $LiMnPO_4$ and $LiFePO_4$ were the result of mixed metal centers in the MO_6 octahedrons. The similar ionic radii of Fe^{2+} and Mn^{2+} and similar structures of $LiMnPO_4$ and $LiFePO_4$ enabled the Fe-substituted $LiMn_{0.7}Fe_{0.3}PO_4$ to be formed as a solid solution of $LiMnPO_4$ and $LiFePO_4$. This solid solution will, however, have an average metal−oxygen bond length longer than that of $LiFePO_4$ but shorter than that of $LiMnPO_4$. The decrease in the average metal−oxygen bond length from $LiMnPO_4$ to $LiMn_{0.7}Fe_{0.3}PO_4$ as well as the higher electronegativity of Fe will reduce the ionic character of the Mn−O bond, causing a negative shift in the $Mn^{3+/2+}$ equilibrium electrode potential. As a result, the Fe^{3+}/Fe^{2+} redox couple would shift to a slightly higher potential and the Mn^{3+}/Mn^{2+} redox couple, to a slightly lower potential. In comparison with $LiMnPO_4/C$, the Fe-substituted $LiMn_{0.7}Fe_{0.3}PO_4/C$ was able to oxidize Mn^{2+} to Mn^{3+} at a lower potential (observed). Improvements in the electrode kinetics could therefore be expected. The narrower Mn^{3+}/Mn^{2+} peak separation in $LiMn_{0.7}Fe_{0.3}PO_4/C$ confirms the greater thermodynamic

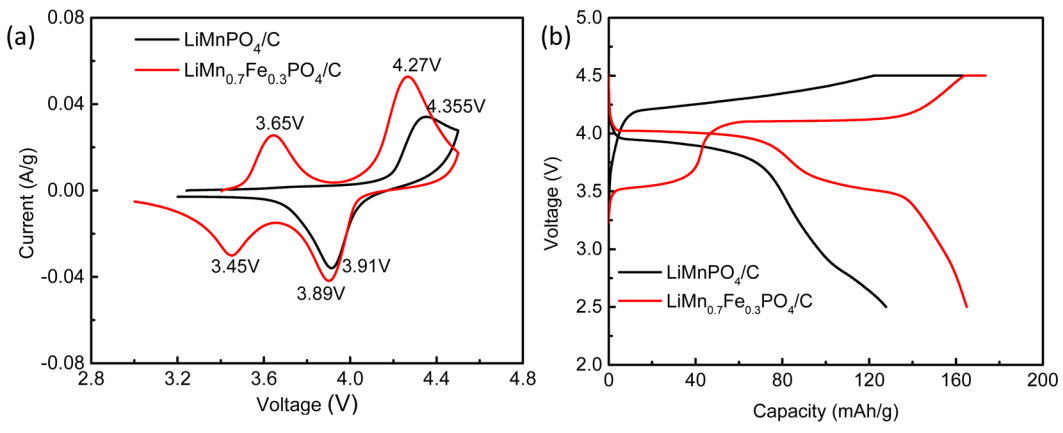

Figure 3. (a) Voltammograms and (b) voltage profiles for $LiMnPO_4/C$ and $LiMn_{0.7}Fe_{0.3}PO_4/C$.

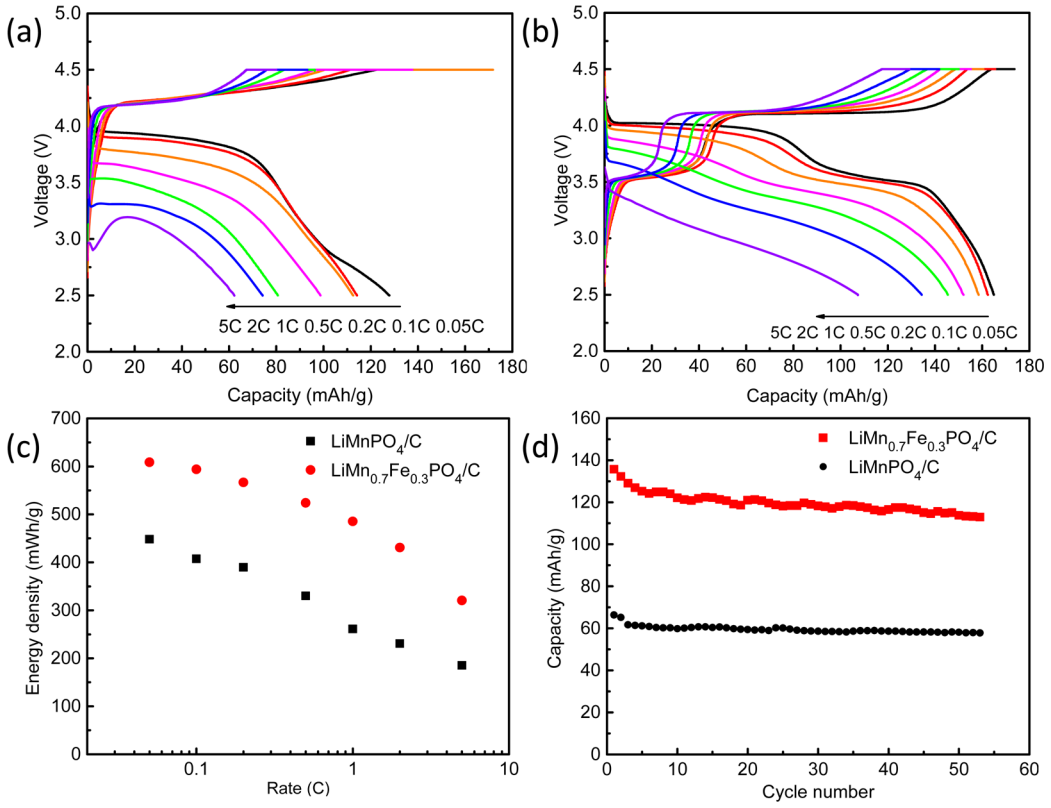

Figure 5. Rate performance of (a) $LiMnPO_4/C$ and (b) $LiMn_{0.7}Fe_{0.3}PO_4/C$. (c) Plots of gravimetric energy density against C rate. (d) Cycling performance of $LiMnPO_4/C$ and $LiMn_{0.7}Fe_{0.3}PO_4/C$ at 0.5 C.

reversibility in Li^+ deintercalation and intercalation reactions. The integrated peak area was also larger than that of $LiMnPO_4$/C and hence a higher charge storage capability was made possible after Fe-substitution. Because all other material parameters were identical, the increase in the reversibility and charge-storage capability of $LiMn_{0.7}Fe_{0.3}PO_4/C$ should be a direct consequence of Fe substitution.

The results of cyclic voltammetry suggested that $LiMn_{0.7}Fe_{0.3}PO_4/C$ should provide a better charge/discharge performance. The prediction was verified by the first-cycle charge and discharge curves in Figure 3b. There were two major causes of polarization: (1) activation polarization (determined by the charge-transfer kinetics of the surface electrochemical process) at the beginning of the discharge and (2) resistance in solid-state Li^+ diffusion characterized by the sharp voltage drop near the end of discharged. The discharge curve of $LiMn_{0.7}Fe_{0.3}PO_4/C$ contained a flat voltage plateau at 4.1 V and a slightly inclined plateau at 3.5 V, corresponding to the $Mn^{3+/2+}$ and $Fe^{3+/2+}$ redox reactions, respectively. For $LiMnPO_4/C$, there was only one voltage plateau around 4.1 V for the $Mn^{3+/2+}$ reaction and a long sloping discharge curve thereafter. The polarization between the charge and discharge voltage plateaus of $LiMn_{0.7}Fe_{0.3}PO_4/C$ was about 0.1 V, which compares very favorably to that of $LiMnPO_4/C$ (0.44 V). This is an indication of the greater reversibility of $LiMn_{0.7}Fe_{0.3}PO_4$/C because of an overall improvement in the surface charge-transfer process in the electrode. The lower capacity of $LiMnPO_4/C$ relative to $LiMn_{0.7}Fe_{0.3}PO_4/C$ is another indication of Li^+ diffusion polarization caused by more sluggish electron and ion transport. The Li^+ storage capacity was also higher in $LiMn_{0.7}Fe_{0.3}PO_4/C$, providing 164 mAh/g at the 0.05 C rate; whereas the corresponding value for $LiMnPO_4/C$ was only 130 mAh/g. Although the substitution of 30 atom % Mn with Fe would reduce the theoretical energy density because of a shorter 4 V region, $LiMn_{0.7}Fe_{0.3}PO_4/C$ still delivered a higher capacity experimentally than $LiMnPO_4/C$ in the 4 V region. It is well-accepted that Li^+ and electron transport are coupled processes during the lithiation/delithiation of nanocrystals.[28] Hence, Fe substitution must have contributed to the improvements in the transport (electronic and ionic) properties of the nanocrystals.

The improvements in electrochemical performance because of Fe substitution were also evident in electrochemical impedance spectroscopic (EIS) measurements. The Nyquist plot of impedance in Figure 4 shows a smaller semicircle for $LiMn_{0.7}Fe_{0.3}PO_4/C$ (a diameter of 280 Ω compared with a diameter of 800 Ω for $LiMnPO_4/C$). Given that both electrodes contained similar amounts of carbon and a similar nanocrystal size, the decrease in the charge-transfer resistance (the size of the semicircle) had to be caused by Fe substitution. Fe substitution also enriched the nanocrystal surface with more reactive $Fe^{3+/2+}$ and $Mn^{3+/2+}$ redox centers than $Mn^{3+/2+}$ centers in pristine $LiMnPO_4$. The faster exchange of Li^+ between the nanocrystals and the electrolyte could then contribute to a higher power capability.

Figure 5a,b shows the rate performance of $LiMnPO_4/C$ and $LiMn_{0.7}Fe_{0.3}PO_4/C$ in discharge. The cells in all of these runs were charged by a CC−CV protocol: 0.05 C to 4.5 V followed by potentiostatic charging at 4.5 V until the current decreased to 0.01 C. The specific discharge capacities of $LiMn_{0.7}Fe_{0.3}PO_4$/C determined as such were 164 mAh/g at the 0.05 C rate and 107 mAh/g at the 5 C rate. The corresponding specific discharge capacities of $LiMnPO_4/C$ were inferior: 127 mAh/g at 0.05 C and 62 mAh/g at 5 C. When these values were

dx.doi.org/10.1021/am403991f | ACS Appl. Mater. Interfaces 2013, 5, 12120−12126

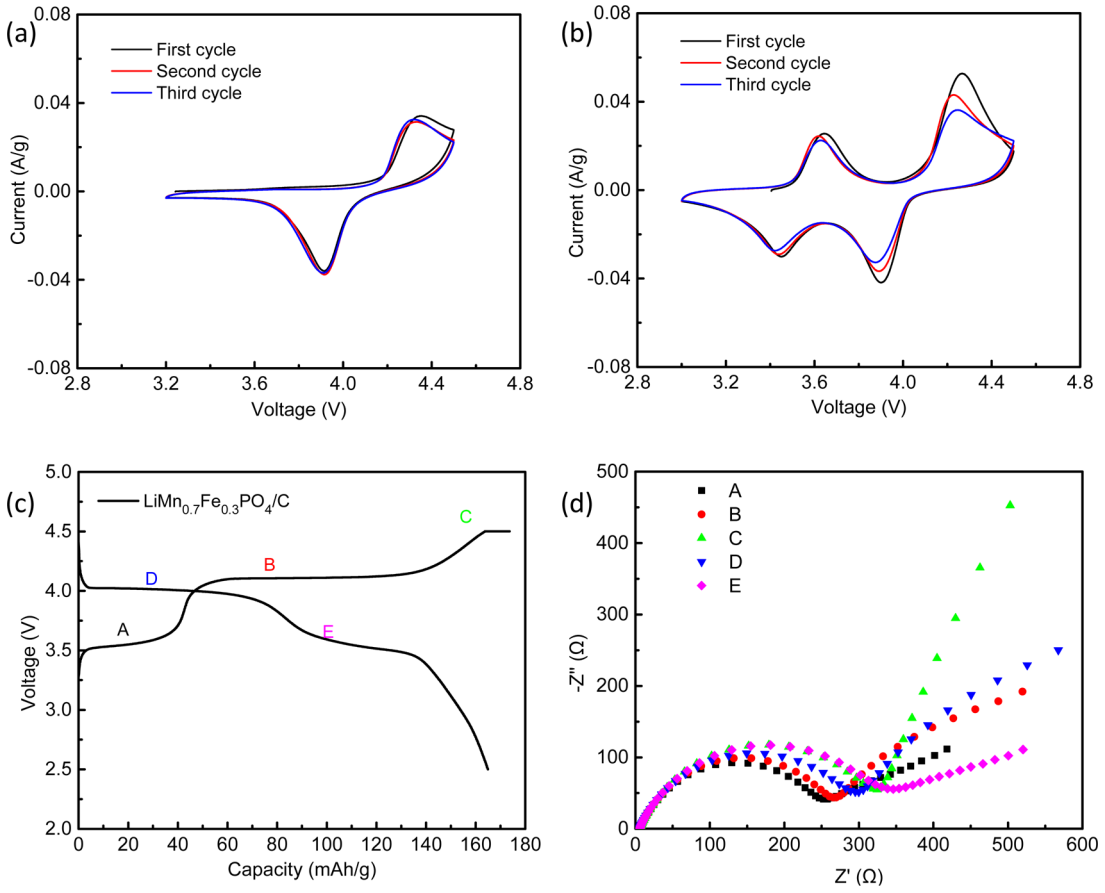

Figure 6. Cyclic voltammograms of (a) $LiMnPO_4$/C and (b) $LiMn_{0.7}Fe_{0.3}PO_4$/C at 0.05 mV/s. (c) First cycle of the charge and discharge profiles at 0.05 C. (d) Nyquist plots at different states of charge and discharge corresponing to the sampling points in panel c.

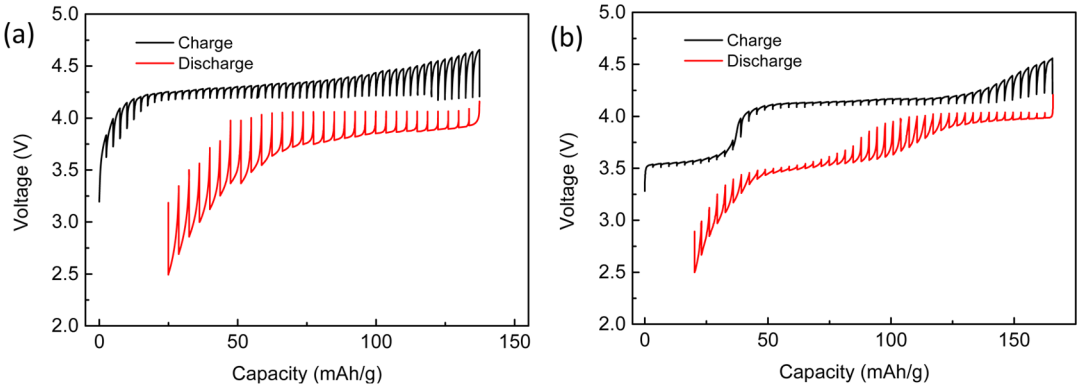

Figure 7. GITT plots of (a) $LiMnPO_4$/C and (b) $LiMn_{0.7}Fe_{0.3}PO_4$/C.

converted to gravimetric energy densities, as shown in Figure 5c, $LiMn_{0.7}Fe_{0.3}PO_4$/C was able to store 608 mWh/g of energy in the phospho-olivine crystal structure. $LiMn_{0.7}Fe_{0.3}PO_4$/C also demonstrated good energy-storage capability over a wide range of discharge rates from 0.05 to 5 C. The high energy density of $LiMn_{0.7}Fe_{0.3}PO_4$/C makes it a better candidate than its sibling $LiFePO_4$ for large-scale energy storage. The energy stored in $LiMn_{0.7}Fe_{0.3}PO_4$/C was nearly double that of $LiMnPO_4$/C at the 5 C rate. This good power performance could again be attributed to Fe substitution being an effective way to elevate the electrochemical performance of $LiMnPO_4$. The cycle stability of $LiMn_{0.7}Fe_{0.3}PO_4$/C was evaluated at 0.5 C charge and discharge rates. Figure 5d shows that both phospho-olivines cycled very well, but $LiMn_{0.7}Fe_{0.3}PO_4$/C still provided twice as much capacity as that of $LiMnPO_4$/C at the end of the 50th cycle. Capacity fading was, however, present in the first few cycles of charge and discharge of $LiMnPO_4$/C and $LiMn_{0.7}Fe_{0.3}PO_4$/C.

Capacity fading was also observed by cyclic voltammetry during the first few cycles of charge and discharge. The decrease in the integrated peak areas in Figure 6a,b is typical of irreversibility associated with passive surface film formation, possibly caused by electrolyte decomposition at high voltages.[14] The impedance changes after charging and discharging to different depths of charge and discharge were also measured to gain further insights into the origin of capacity fading. As shown

dx.doi.org/10.1021/am403991f | ACS Appl. Mater. Interfaces 2013, 5, 12120−12126

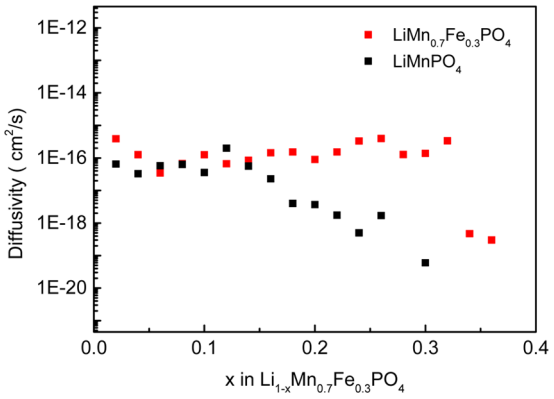

Figure 8. Li^+ diffusivity as a function of lithium composition.

in Figure 6c,d, constant potential charging at 4.5 V increased the size of the semicircle in the EIS plot, indicating the increase in the charge-transfer resistance of the electrode reaction. This could be caused by electrolyte decomposition and solid electrolyte interphase deposition because of extended operation at voltages higher than the stability limit of the electrolyte.

The analysis of the voltage profile after a series of current pulses using the Galvanostatic intermittent titration technique (GITT) could provide a wealth of information about the electrode reaction. Generally, fast voltage relaxation and low polarization (the difference between the voltage immediately after the application of the current pulse and the stabilized voltage after the removal of the current pulse) indicate facile reaction kinetics and vice versa. The GITT measurements in Figure 7 clearly show that polarization was smaller in $LiMn_{0.7}Fe_{0.3}PO_4/C$ than in $LiMnPO_4/C$ and hence the electrode reaction was more facile for the former. The reactions in charge and discharge involve two consecutive processes: the extraction of Li^+ from and insertion of Li^+ into the phospho-olivine nanocrystals and the solvation/desolvation of Li^+ at the electrolyte-electrode interface. It is known that electron conduction in bulk $LiMPO_4$ (M = Fe and Mn) is dominated by polaron hopping.[26,27] Because the energy barrier to polaron hopping is lower in $LiFePO_4$,[26] the partial substitution of Mn in $LiMnPO_4$ by Fe should reduce the polaron hopping barrier in $LiMnPO_4$ to some extent. At the same time, Fe substitution could also decrease the Jahn–Teller distortion around Mn^{3+} that hinders Li^+ transport in the nanocrystal. Hence, Fe substitution could simultaneously improve electron and Li^+ diffusion in the bulk of the solid state. Being a solid solution, $LiMn_{0.7}Fe_{0.3}PO_4/C$ also provides a Fe-enriched surface where Li^+ exchange with the electrolyte is more facile. Therefore, delithiation and lithiation were also expedited at the surface. Interestingly, $LiMn_{0.7}Fe_{0.3}PO_4/C$ displayed a sloping open-circuit voltage envelope in the 3.5 V region (Figure 7b). This suggests that, contrary to the common two-phase mechanism for the reaction between Li^+ and $LiMPO_4$, there exists the possibility of a single-phase reaction occurring in the 3.5 V region for $LiMn_{0.7}Fe_{0.3}PO_4/C$. This finding is consistent with recent ab initio calculations of the $LiMn_{1-x}Fe_xPO_4$ system.[25] Normally, the nucleation of a new phase in the two-phase reaction mechanism is induced by Li^+–M^{2+} or V_{Li+}–M^{3+} attractive interactions.[29] When Li is progressively delithiated or lithiated, there is an increase in strongly repulsive V_{Li+}–Mn^{2+} (or Li^+–Mn^{3+}) interaction to hinder nucleation during charging and discharging, respectively. For $LiMn_{0.7}Fe_{0.3}PO_4/C$, the decrease in the driving force for the nucleation of the second phase (Li^+–Fe^{2+} or V_{Li+}–Fe^{3+} interaction) is the reason for reactions in a single phase near the Fe^{2+}/Fe^{3+} redox potential. However, the driving force for phase separation in the 4.1 V region remained large for several reasons: (1) stronger electron localization on Mn, (2) larger lattice mismatch between the MPO_4 and $LiMPO_4$ phases, and (3) reduction in the Fe dilution effects on Mn and hence less repulsive forces against phase separation.

Figure 8 shows some indicative Li^+ diffusivities calculated from the GITT measurements for $x = 0$ to 0.38 in $Li_{1-x}Mn_{0.7}Fe_{0.3}PO_4$ where reactions in the single phase prevailed. Diffusivity was also estimated from GITT beyond this region. The results show that the lithium diffusivity for lithium extraction from $x = 0$ to 0.34 was of the order of 10^{-16} cm^2/s and varied very little with Li^+ concentration. There was, however, an abrupt decline in diffusivity at x greater than 0.34. This is indication of the more facile diffusion of Li^+ in the single-phase reaction relative to the two-phase reaction, which became significant at $x > 0.34$. For $Li_{1-x}MnPO_4$ without Fe substitution, a smaller single-phase reaction region from $x = 0$ to 0.15 was observed. Beyond this composition, lithium diffusivity also decreased sharply with the intrusion of the two-phase reaction. The presence of a one-phase region in $Li_{1-x}MnPO_4$ could be originated from the size-dependent reduction of the miscibility gap between the two end members of phospho-olivines (i.e., larger x values for small nanocrystals). Li^+ diffusivity measurements beyond $x = 0.38$ for $Li_{1-x}Mn_{0.7}Fe_{0.3}PO_4$ and $x = 0.3$ for $Li_{1-x}MnPO_4$ did not result in reliable values because of equipment limitations.

CONCLUSIONS

High-performance $LiMn_{0.7}Fe_{0.3}PO_4/C$ was synthesized by a scalable process involving high-energy ball-milling and solid-state synthesis. Carbon was present as a uniform coating and also as embedded current collectors to lower the external resistance to electron transport. A 30% Fe-substituted $LiMn_{0.7}Fe_{0.3}PO_4/C$ composite delivered exemplary power performance. Through a combination of different material characterization methods, it was concluded that Fe substitution significantly improved Li^+ and electron transport in the bulk as well as charge transfer on the surface of the nanocrystals. The electrochemical activity of Mn was enhanced through decreasing the ionic character of Mn ions by substitution with more electronegative Fe ions. In particular, the appearance of a large single-phase reaction region supported fast Li^+ extraction/insertion. All of these factors worked in tandem to enhance the energy and power densities of Fe-substituted $LiMnPO_4$.

ASSOCIATED CONTENT

Supporting Information

Thermal gravimetric analysis of $LiMnPO_4/C$ and $LiMn_{0.7}Fe_{0.3}PO_4/C$. This material is available free of charge via the Internet at http://pubs.acs.org.

AUTHOR INFORMATION

Corresponding Authors

*E-mail: luli@nus.edu.sg (L.L.).

*E-mail: cheleejy@nus.edu.sg; Fax: 65 67791936; Tel.: 65 6516 2899 (J.Y.L.).

Notes

The authors declare no competing financial interest.

■ ACKNOWLEDGMENTS

This work was supported by the National University of Singapore Graduate School for Integrative Science and Engineering (NGS).

■ REFERENCES

(1) Delacourt, C.; Poizot, P.; Morcrette, M.; Tarascon, J. M.; Masquelier, C. *Chem. Mater.* **2004**, *16*, 93−99.
(2) Dominko, R.; Bele, M.; Gaberscek, M.; Remskar, M.; Hanzel, D.; Goupil, J. M.; Pejovnik, S.; Jamnik, J. *J. Power Sources* **2006**, *153*, 274−280.
(3) Delacourt, C.; Laffont, L.; Bouchet, R.; Wurm, C.; Leriche, J. B.; Morcrette, M.; Tarascon, J. M.; Masquelier, C. *J. Electrochem. Soc.* **2005**, *152*, A913−A921.
(4) Martha, S. K.; Markovsky, B.; Grinblat, J.; Gofer, Y.; Haik, O.; Zinigrad, E.; Aurbach, D.; Drezen, T.; Wang, D.; Deghenghi, G.; Exnar, I. *J. Electrochem. Soc.* **2009**, *156*, A541−A552.
(5) Martha, S. K.; Grinblat, J.; Haik, O.; Zinigrad, E.; Drezen, T.; Miners, J. H.; Exnar, I.; Kay, A.; Markovsky, B.; Aurbach, D. *Angew. Chem., Int. Ed.* **2009**, *48*, 8559−8563.
(6) Wang, Y.; Wang, J.; Yang, J.; Nuli, Y. *Adv. Funct. Mater.* **2006**, *16*, 2135−2140.
(7) Brunetti, G.; Robert, D.; Bayle-Guillemaud, P.; Rouviere, J. L.; Rauch, E. F.; Martin, J. F.; Colin, J. F.; Bertin, F.; Cayron, C. *Chem. Mater.* **2011**, *23*, 4515−4524.
(8) Chung, S. Y.; Choi, S. Y.; Lee, S.; Ikuhara, Y. *Phys. Rev. Lett.* **2012**, *108*, 195501−195504.
(9) Sharma, N.; Guo, X. W.; Du, G. D.; Guo, Z. P.; Wang, J. Z.; Wang, Z. X.; Peterson, V. K. *J. Am. Chem. Soc.* **2012**, *134*, 7867−7873.
(10) Zhong, G. B.; Wang, Y. Y.; Zhang, Z. C.; Chen, C. H. *Electrochim. Acta* **2011**, *56*, 6554−6561.
(11) Burba, C. A.; Frech, R. *J. Power Sources* **2007**, *172*, 870−876.
(12) Yu, J. G.; Rosso, K. M.; Liu, J. *J. Phys. Chem. C* **2011**, *115*, 25001−25006.
(13) Gwon, H.; Seo, D. H.; Kim, S. W.; Kim, J.; Kang, K. *Adv. Funct. Mater.* **2009**, *19*, 3285−3292.
(14) Wang, D. Y.; Buqa, H.; Crouzet, M.; Deghenghi, G.; Drezen, T.; Exnar, I.; Kwon, N. H.; Miners, J. H.; Poletto, L.; Graetzel, M. *J. Power Sources* **2009**, *189*, 624−628.
(15) Bakenov, Z.; Taniguchi, I. *Electrochem. Commun.* **2010**, *12*, 75−78.
(16) Koleva, V.; Stoyanova, R.; Zhecheva, E. *Mater. Chem. Phys.* **2010**, *121*, 370−377.
(17) Oh, S. M.; Oh, S. W.; Yoon, C. S.; Scrosati, B.; Amine, K.; Sun, Y. K. *Adv. Funct. Mater.* **2010**, *20*, 3260−3265.
(18) Doan, T. N. L.; Taniguchi, I. *J. Power Sources* **2011**, *196*, 1399−1408.
(19) Kim, J.; Seo, D. H.; Kim, S. W.; Park, Y. U.; Kang, K. *Chem. Commun.* **2010**, *46*, 1305−1307.
(20) Luo, S.; Wang, K.; Wang, J.; Jiang, K.; Li, Q.; Fan, S. *Adv. Mater.* **2012**, *24*, 2294−2298.
(21) von Hagen, R.; Lorrmann, H.; Moller, K. C.; Mathur, S. *Adv. Energy Mater.* **2012**, *2*, 553−559.
(22) Wang, H. L.; Yang, Y.; Liang, Y. Y.; Cui, L. F.; Casalongue, H. S.; Li, Y. G.; Hong, G. S.; Cui, Y.; Dai, H. J. *Angew. Chem., Int. Ed.* **2011**, *50*, 7364−7368.
(23) Yamada, A.; Takei, Y.; Koizumi, H.; Sonoyama, N.; Kanno, R. *Appl. Phys. Lett.* **2005**, *87*, 252503-1−252503-3.
(24) Yamada, A.; Chung, S. C. *J. Electrochem. Soc.* **2001**, *148*, A960−A967.
(25) Malik, R.; Zhou, F.; Ceder, G. *Phys. Rev. B* **2009**, *79*, 214201-1−212401-7.
(26) Ellis, B.; Perry, L. K.; Ryan, D. H.; Nazar, L. F. *J. Am. Chem. Soc.* **2006**, *128*, 11416−11422.
(27) Chen, G.; Richardson, T. J. *J. Power Sources* **2010**, *195*, 1221−1224.
(28) Xiao, J.; Chernova, N. A.; Upreti, S.; Chen, X.; Li, Z.; Deng, Z.; Choi, D.; Xu, W.; Nie, Z.; Graff, G. L.; Liu, J.; Whittingham, M. S.; Zhang, J.-G. *Phys. Chem. Chem. Phys.* **2011**, *13*, 18099−18106.
(29) Seo, D.-H.; Gwon, H.; Kim, S.-W.; Kim, J.; Kang, K. *Chem. Mater.* **2009**, *22*, 518−523.